Design and Implementation of a Power Smoothing System for Cross-flow Current Turbines

Hannah Aaronson

A thesis submitted
in partial fulfillment of the
requirements for the degree of

Master of Science

University of Washington

2019

Reading Committee:

Brian Polagye, Chair

Brian Johnson

Brian Fabien

Robert J. Cavagnaro

Program Authorized to Offer Degree:
Department of Mechanical Engineering

University of Washington

Abstract

Design and Implementation of a Power Smoothing System for Cross-flow Current Turbines

Hannah Aaronson

Chair of the Supervisory Committee:
Associate Professor Brian Polagye
Department of Mechanical Engineering

Previous studies optimizing control strategies for cross-flow (i.e., "vertical-axis") current turbines found that sinusoidally varying rotor speed within a single rotation can increase mechanical power output by up to 59%. However, this control strategy, known as intracycle control, comes with a cost: for a two-bladed turbine, electrical power output associated with a 1 kW average is estimated to fluctuate between producing 16 kW and consuming 11 kW twice per rotation. This power quality is incompatible with direct use. Here, we describe a power smoothing system that reduces the root mean square of fluctuating output power by 99% with 97.0% efficiency, using a simple LC filter and bi-directional DC-DC converter. A small-scale simulation of the system is validated using a comparably sized experimental set-up to increase confidence in the full-scale simulation and demonstrate practical implementation.

TABLE OF CONTENTS

LIST OF FIGURES

LIST OF TABLES

ACKNOWLEDGMENTS

Chapter 1

INTRODUCTION

One of the largest challenges for the electrical integration of distributed renewable resources is power fluctuation over relatively short and long time scales [1]. Intermittent and unpredictable power from renewable resources, used to offset climate change associated with dispatchable fossil-fuel resources, may disrupt the stability of the power grid and the balance of supply and demand. Long-term power intermittency is a well-established concern in the renewable energy industry, and the feasibility of grid-scale energy storage systems (e.g., pumped hydropower, compressed-air storage) to mitigate this is an active area of research [2], [3]. Short-term power fluctuation is also problematic. For example, in wind energy generation, incident resource power is proportional to the cube of wind speed, such that turbulent gusts can lead to grid frequency disruption or voltage flicker. In such power generation systems, a bi-directional DC-DC converter on the DC bus, coupled with energy storage (e.g., batteries, supercapacitors, or flywheels) can smooth these minute-to-minute variations in power [4].

Like generation from other renewable resources, current turbines operating in rivers, tidal channels, and ocean boundary currents will be required to adhere to distribution and transmission grid standards [5]. To date, a relatively high levelized cost of energy in comparison to alternatives has limited the adoption of grid-scale current turbine arrays. However, in remote locations, conventional energy costs are higher and current turbines may be cost-effective [6]. These remote locations are often isolated from utility-scale grid infrastructure, which makes power quality of electrical generation a particular concern [7].

Cross-flow turbines ("vertical-axis" in wind) have distinct, potentially advantageous properties compared to axial-flow turbines ("horizontal-axis"), including lower maximum blade

speed, bi-directional functionality in reversing tidal flows, and potential to increase system efficiency in tightly-packed, high-blockage arrays [8], [9]. Typical control strategies involve maintaining an optimal tip-speed ratio for a given inflow velocity through regulation of rotor speed or torque. Turbines with a high mechanical conversion efficiency (i.e., water velocity to shaft torque) typically have a small number of straight blades [10]. Because of the variation in apparent angle of attack for the rotating blades, hydrodynamic torque varies periodically with blade position, leading to oscillations in mechanical power over the course of a single rotation, with a primary frequency dictated by the number of turbine blades. This instantaneous power cycles between production (generating) and consumption (motoring) in the range of practical interest for net power generation [11], [12]. Furthermore, it has been demonstrated that optimizing the amplitude and frequency of turbine speed within a rotation, termed "intracycle control", can increase mechanical conversion efficiency by up to 59% [13]. However, this increases the peak-to-average ratio of mechanical power, such that the associated electrical power may not be compatible with direct use [14].
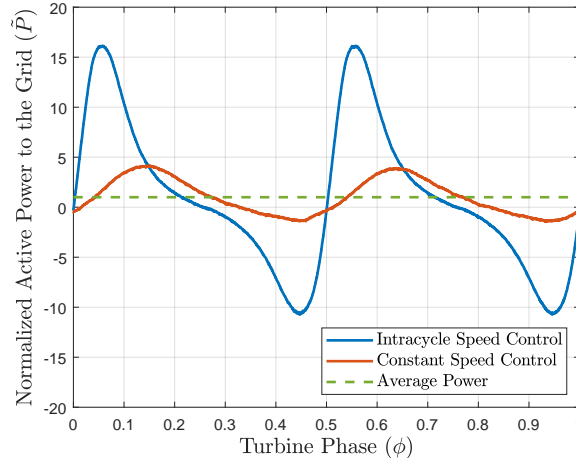

Figure 1.1: Normalized active power as a function of rotational phase for a current turbine utilizing differing control schemes.

Fig. 1.1 compares the active power delivered to the grid, normalized by average power, for a two-bladed turbine rotating at ~1 Hz utilizing constant speed or intracycle control.

For equivalently-sized turbines, intracycle control increases the average power, but instantaneous power is characterized by large peak-to-peak power ratio (>25) and periodic power consumption. If integrated with a weak grid, such low power quality could disrupt grid stability.

The design and implementation of a power smoothing system (PSS) and control scheme to mitigate these fluctuations is presented in this work. Such a system allows the turbine to be optimized for average power output, thus potentially reducing cost of energy, while still delivering stable, high-quality power to an end use. As turbine rotation rates are on the order of one revolution per second, supercapacitors controlled by a power converter are more appropriate to smooth power than batteries, and have additional advantages including a long life span and high energy storage efficiency [15]. Supercapacitors are not economic for smoothing power on time scales longer than a minute, so power fluctuations over longer time scales, such as variations in tidal currents, require energy-dense approaches capable of long deep-discharge life cycles [16].

Prior work on similar topics includes simulation of a capacitor-based power smoothing system on the DC bus for smoothing short-term power fluctuation from axial-flow wind turbines due to variation in wind speed [17], [18]. However, axial-flow turbines produce only positive electrical power with a peak-to-average ratio much lower than power produced from the cross-flow turbine shown in Fig. 1.1. Further, neither of these studies were validated experimentally. In this work, the PSS design is first constructed in simulation and designed to optimize output power quality from a cross-flow turbine while minimizing power loss, size, complexity, and cost. A bench-top hardware system, sized to approximately match the power expected from a laboratory-scale turbine, is used to validate simulation results. Once the simulation is validated using experimental data, the performance and feasibility of a larger-scale system is considered.

Chapter 2

METHODS

The power smoothing system, integrated on the DC bus of a generator-to-grid power collection scheme, is shown schematically in Fig. 2. The instantaneous active power shown in Fig. 1.1 is measured at the three-phase intersection with the grid, shown in green, without the use of the PSS system on the DC bus. The inputs to the system are a time series of the expected turbine rotational rate and hydrodynamic torque, based on non-dimensional performance coefficients [14].
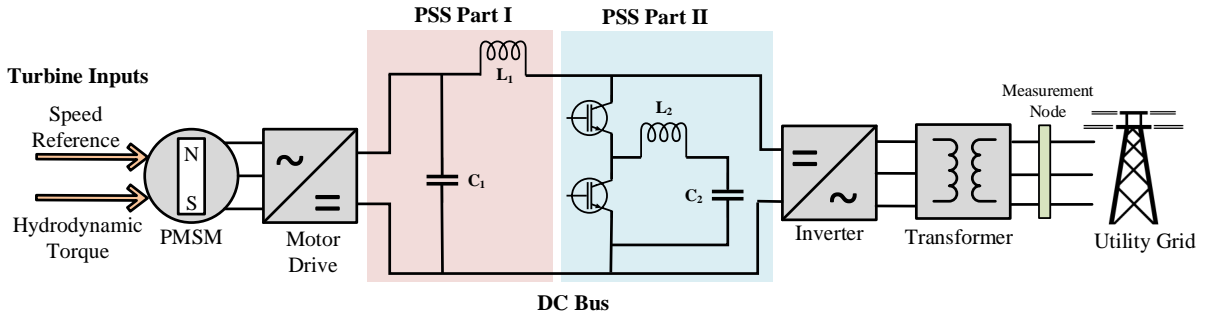
Figure 2.1: Generator-to-grid power collector simulation layout including the proposed power smoothing system (PSS).

The proposed PSS is the combination of an LC filter and a bi-directional DC-DC converter utilizing Proportional-Integral current control. The LC filter (PSS Part I) is sized to smooth rapidly switching current on the DC bus arising from the motor drive control system which regulates turbine rotation. The LC filter attenuates high frequency fluctuations in DC bus current and yields low frequency, low amplitude current. Next, the DC-DC converter (PSS Part II) regulates current through the output inductor and capacitor to eliminate residual power oscillation.

2.1 System Design

The cut-off frequency of the low pass filter in PSS Part I is given by,

$$f_c = \frac{1}{2\pi\sqrt{L_1 C_1}} \tag{2.1}$$

where L_1 is inductance and C_1 is capacitance. This attenuates frequencies above f_c at a rate of -20 dB/decade. The capacitor is approximately sized based on the cyclic energy E produced from the turbine, given by,

$$E = \frac{1}{2}C_1 V^2 \tag{2.2}$$

where V is the voltage across C_1. To achieve a desired cut-off frequency, maximizing C and minimizing L reduces equivalent series resistance (ESR) in the circuit. A large capacitor has the added benefit of stabilizing the voltage input to the motor drive, but this must be balanced against relatively high component cost [16].

Part II of the power smoothing system takes the low frequency filtered current from Part I and removes the remaining sinusoidal fluctuations such that final power output is constant in time. This is achieved by a bi-directional DC-DC converter, where the inductor and capacitor (L_2 and C_2) serve as short-term energy storage components. The duty cycle on the switches to the converter are dictated by the control strategy shown in Fig. 2.2. This control strategy was adapted from a comparable system designed to smooth highly dynamic power draw from a metal forming machine tool [19].

To implement this control strategy, two current and two voltage sensors are needed, as shown in Fig. 2.9. I_{L1} and V_{bus} are used to calculate the instantaneous power P_{DC} on the DC bus. A low pass filter (LPF) calculates the running average power, $\overline{P}_{DC}$ - the desired constant power output from the DC-DC converter. The difference between average and instantaneous power P_{ref} is absorbed by the PSS. The quotient of P_{ref} and the capacitor voltage V_{C2} gives the current to be demanded through the inductor, I_{ref}. I_{ref} is compared to the measured inductor current I_{L2}, and the difference between the two is the PI controller's

error metric. This controller calculates a duty ratio D to synchronously control the converter switches at frequency f_{sw}. This control strategy can be summarized by

$$I_{ref} = \frac{P_{ref}}{V_{C2}} = \frac{I_{L1}V_{bus} - \overline{P}_{DC}}{V_{C2}} \tag{2.3}$$

$$D = (I_{ref} - I_{L2})\left(k_p + \frac{k_i}{s}\right). \tag{2.4}$$
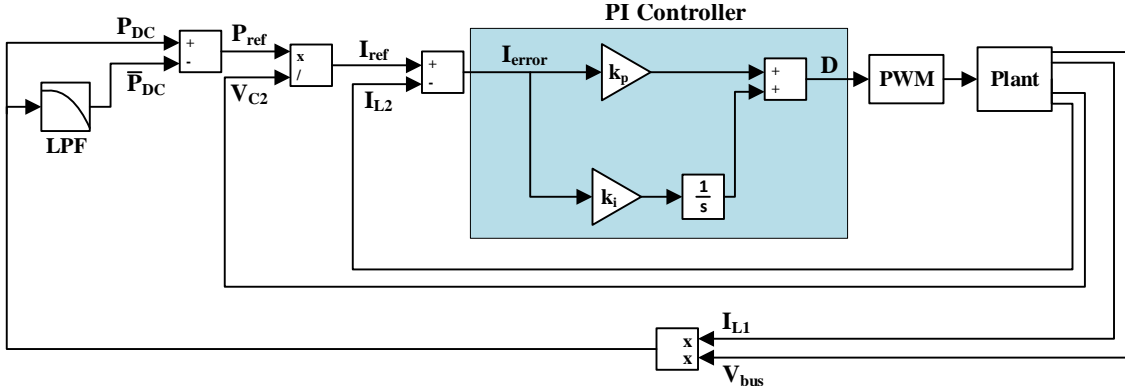
Figure 2.2: Layout of the controller used in PSS Part II. Terms are defined in the narrative.

A pulse width modulation (PWM) scheme uses D to create gating signals which dictate the percentage of time the top switch is on, as compared to the bottom switch, for each cycle. These gating signals control the dynamics of the physical system (i.e., "plant" in Fig. 2.2).

Controller gains k_p and k_i are based on the complementary sensitivity function, $T(s)$, defined in terms of an open loop transfer function $l(s)$ [20] as

$$T(s) = \frac{l(s)}{1 + l(s)} = \frac{k_i}{L_2} \frac{1 + \frac{k_p}{k_i}s}{s^2 + \frac{1}{L_2}(R_{L2} + k_i)s + \frac{k_p}{L_2}}. \tag{2.5}$$

$l(s)$ is defined using $G_{iu}(s)$, a transfer function relating current to voltage across L_2 (including its equivalent series resistance R_{L2}), and $G_c(s)$, the PI controller transfer function, given by

$$l(s) = G_{iu}(s)G_c(s) = \left(\frac{1}{sL_2 + R_{L2}}\right)\left(k_p + \frac{k_i}{s}\right). \tag{2.6}$$

T(s) is equated to a canonical second-order system,

$$T(s) = T_o\omega_o^2 \frac{1 + \omega_z s}{s^2 + 2\xi\omega_o s + \omega_o^2} \tag{2.7}$$

which is characterized by controller damping ratio ξ and controller bandwidth ω_o. By equating Eqns. (2.5) and (2.7), k_p and k_i are calculated as

$$k_i = \omega_o^2 L_2 \tag{2.8}$$

$$k_p = 2\xi\omega_o L_2 - R_{L2}. \tag{2.9}$$

2.2 Bench-Top Set-Up

The topology used to validate a small-scale version of the PSS (e.g., 10 W average power output) is shown in Fig. 2.3. The system is an abstraction of the DC bus in Fig. 2, where the turbine, generator, and motor drive are replaced with an equivalent controllable current source input mimicking turbine electrical power output. The inverter, transformer, and utility grid are emulated by a DC voltage source and a resistive load in parallel. This system is not meant to perfectly emulate a grid-connected turbine; rather it is intended to demonstrate the capability of the PSS.

To determine a time series of data to use as the current source input I_{turb}, first an entirely experimental system was developed, as detailed in Appendix A. However, it proved difficult to extract useful electrical power from the system, due to the inefficiency of power regeneration for the small-scale servomotor and servodrive. Instead, a combination of experimental and simulation data are used, as detailed in Fig. 2.4. First, a laboratory-scale turbine is used to collect experimental measurements of rotation rate ω and hydrodynamic torque τ using a two-bladed turbine in a recirculating flume [13], [21]. The turbine has a projected

frontal area of $0.04\ m^2$, with turbine height and diameter a 1:5 scale of the larger-scale system described in Section 2.3. A servomotor was used for speed control to maintain a tip-speed ratio of 2.16 (maximizing average power output) in an inflow velocity of 1 m/s, giving a rotor rotational rate of 4 Hz.
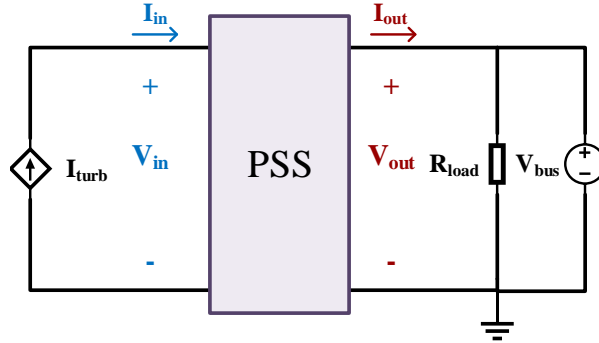
Figure 2.3: Bench-test set-up using a simplified abstraction of the DC bus.
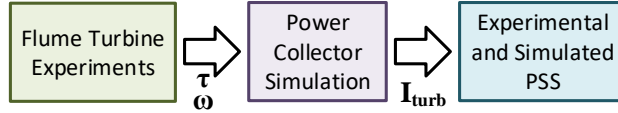
Figure 2.4: Flow chart of systems used to create the input I_{turb} to the PSS.

Next, a simulation of a baseline turbine-to-grid power collection simulation is considered, using experimental turbine speed and hydrodynamic torque as the inputs to the PMSM generator and matching the layout shown in Fig. 2, but without the PSS. The simulation, implemented in Matlab Simulink, is discussed in further detail in Section 2.3. The characteristics of the simulated generator are modeled after a unit sized for laboratory-scale experiments (Parker SM233AL-KPSM).

Fig. 2.5 shows the mechanical power input to the simulation P_{mech} and the resulting electrical power P_{elec} observed on the DC bus for one turbine rotation. Mechanical power is

$$P_{mech} = \tau\omega \tag{2.10}$$

and the simulated electrical power output is given by

$$P_{elec} = I_{turb}V_{bus} \tag{2.11}$$

where I_{turb} is the current produced by the turbine as observed on the DC bus and V_{bus} is the steady DC bus voltage.
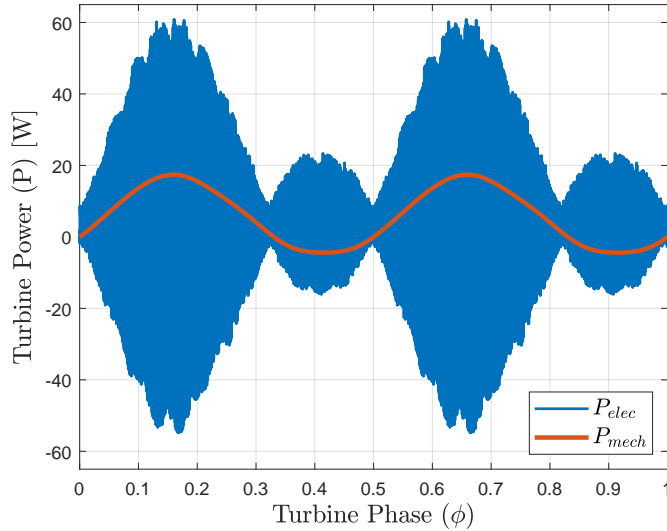
Figure 2.5: Mechanical power of the turbine, characterized by sinusoidally fluctuating torque, and the resulting electrical power on the DC bus.

For this control scheme, ω and V_{bus} are both held constant, such that angular-dependent torque produces time-varying DC bus current to be smoothed by the PSS. All turbines considered in this work are two-bladed, so sinusoidal fluctuations in power occur twice per rotation.

A detailed view of the DC bus current is shown in Fig. 2.6. The polarity of current fluctuates rapidly at the rate of the emulated motor drive switching frequency (20 kHz) enacting speed control, resulting in a discontinuous waveform with a higher peak-to-average

ratio than the turbine mechanical power. This is the current to be programmed as I_{turb}, the input to the PSS system as shown in Fig. 2.3.
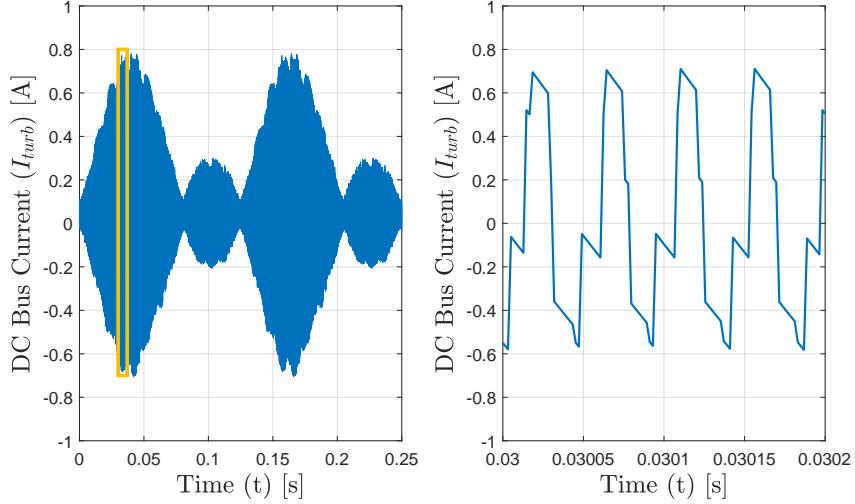
Figure 2.6: Electrical current on the DC bus over one turbine rotation (left) and 0.25° (0.2 ms) of turbine rotation (right).

For the benchtop PSS, this rapidly fluctuating current is provided by an arbitrary function generator (Agilent 33220A). Because it outputs a voltage, not a current, an effective current source is realized using Thẽvenin and Norton circuit equivalents [22]. The voltage source V_N required to produce the desired current input I_{turb} is provided by a high-power operational amplifier, amplifying arbitrary function generator V_{arb} on the inverting input and a constant voltage source V_{ref} on the non-inverting input. The system current input, I_{turb}, is given by

$$I_{turb} = \frac{1}{R_T}(V_N - V_{bus}) \tag{2.12}$$

$$V_N = -\frac{R_f}{R_g}V_{arb} + \left(\frac{R_f}{R_g} + 1\right)\left(\frac{R_1}{R_1 + R_2}\right)V_{ref} \tag{2.13}$$

and shown schematically in Fig. 2.7.
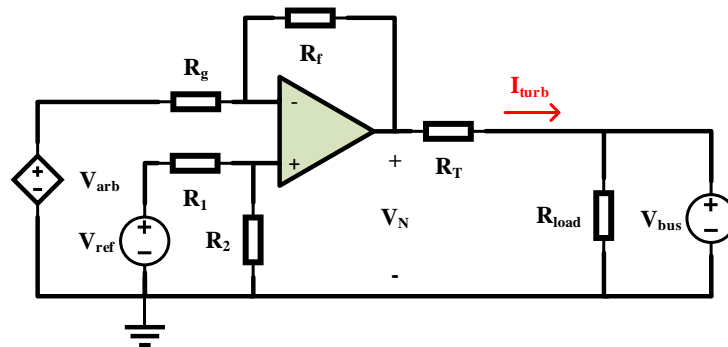
Figure 2.7: Operational amplifier used for the bench-top system set-up.

The bench-top PSS is shown in implementation in Fig. 2.8 and schematically in Fig. 2.9. A summary of all system components and controller parameters is provided in Table 2.1. Inductor ESRs are measured experimentally using a digital multimeter and capacitor values are taken from component data sheets. A DC bus voltage of 80 V is chosen to be consistent with the motor drive selection for this scale of turbine. The cut-off frequency of the PSS I LC filter (150 Hz) is 130x lower than the switching frequency of the input current. Controller bandwidth ω_o is chosen as 500 rad/s (10x the blade pass frequency of the turbine), and the damping ratio is chosen as 0.4. These controller parameters are used to calculate k_p and k_i.
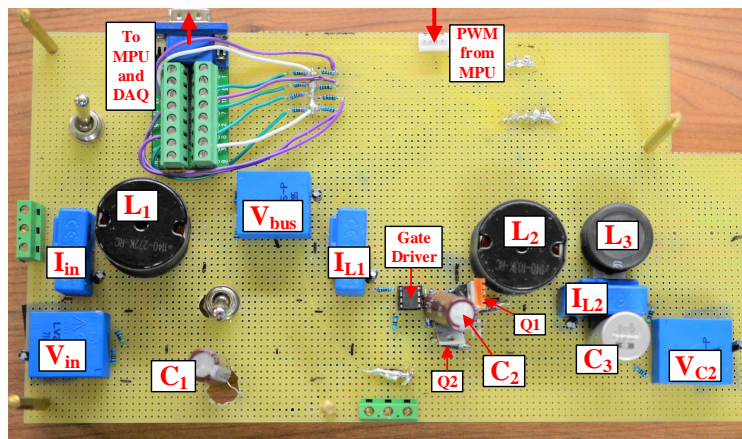
Figure 2.8: Hardware implementation of the PSS on a protoboard.
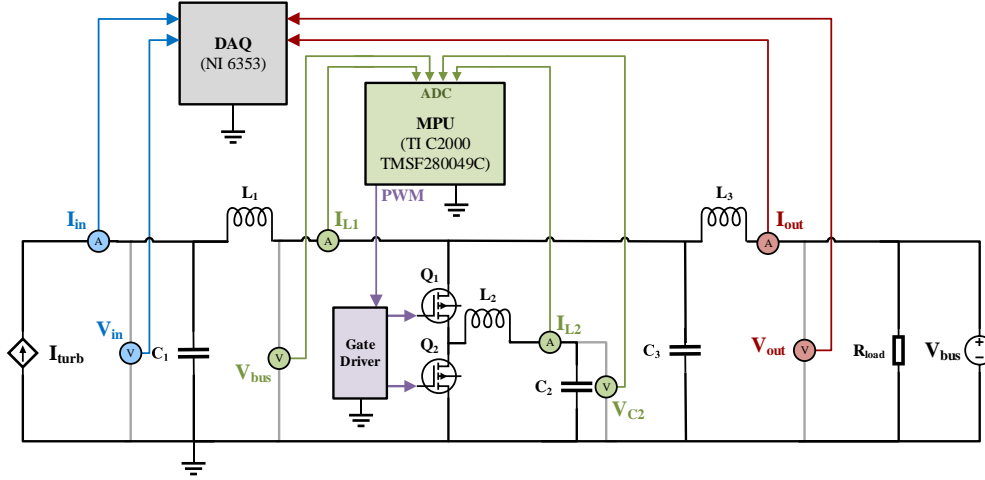
Figure 2.9: Schematic of full PSS bench-top set-up.

Table 2.1: Relevant parameters for the bench-top PSS.

Set-Up Components		PSS Components		
Variable	Value	Variable	Value	ESR [mΩ]
R_f	30 kΩ	L_1	2.7 mH	700
R_g	2 kΩ	L_2	10 mH	1700
R_1	10 kΩ	L_3	1.8 mH	700
R_2	10 kΩ	C_1	390 μF	44
V_{ref}	10 V	C_2	910 μF	26
R_L	10 Ω	C_3	390 μF	44
R_{load}	50 Ω	**Controller Parameters**		
V_{bus}	80 V	f_{sw}	10 kHz	
		k_p	2.3 H/s^2	
		k_i	2500 Ω	

A TI TMS320F280049C microcontroller (MPU) is used on the TI C2000 LaunchXL breakout board with a system clock of 10 ns. A symmetrical triangle carrier at 10 kHz is used for PWM generation, with two current and two voltage measurements sampled at

the analog-to-digial converter (ADC) pins twice per switch cycle, when the carrier signal is high or low. The ADC sample occurs for 10 clock cycles of the MPU. The controller code from Eqns. (2.3) and (2.4) is written in Code Composer Studio and complied onto the MPU. Digital low-pass filters are added to the measurements of V_{bus}, I_{L1}, and V_{C2} to mitigate sensor noise during real-time control. Another LC filter (L_3 and C_3) is added to the output of the bench-top system to filter high-frequency switching noise introduced by the DC-DC converter. This allows for easier observation of the low-frequency smoothing capabilities of the system using raw data in the time domain without post-processing, and does not affect the performance metrics used to evaluate the system. This additional LC filter is not needed for a full-scale grid-integrated system, where power would typically be fed through an inverter on the grid side and converter switching noise on the DC bus would not be observed by grid-side measurements.

Measurements of current (LEM LAH 25-NP) and voltage (LEM LV 25-P) on the input and output of the system are read into a data acquisition device (NI DAQ 6353). Data is acquired at a sample rate of 250 kHz for 50 emulated turbine rotations (12.5 s). This test is repeated 10 times and efficiency is calculated for each trial using

$$\eta = \frac{\overline{P}_{out}}{\overline{P}_{in}}, \tag{2.14}$$

where P_{in} is the product of instantaneous input current and voltage (I_{in} and V_{in}) and and P_{out} is the product of instantaneous output current and voltage (I_{out} and V_{out}). Efficiency is then averaged over all trials.

System performance is evaluated using a periodogram to compute the power spectra of a time series of input and output DC bus electrical power (P_{in} and P_{out}). A periodigram is the absolute value squared of a single-sided fast Fourier transform, normalized by the number of samples in the time series L [23]. Periodograms are computed for all ten trials, then the amplitude of the periodogram P_{PG} (in W^2) from each frequency bin is averaged across all trials (giving $\overline{P}_{PG}$). The root mean square (RMS) of the oscillating component of P_{in} and P_{out} across a specified range of frequencies can be calculated from this averaged power

spectra, using

$$P_{rms} = \sqrt{\frac{\sum_{i=2}^{N}(\overline{P}_{PG,i})}{L-1}} \tag{2.15}$$

where $\overline{P}_{PG,i}$ is the magnitude of the power spectra at each frequency, N is the number of frequencies of interest, and L is the number of data points in the time series. $P_{rms,low}$ is used to denote P_{rms} at low frequencies (i.e., up to 100 Hz). By neglecting contributions of high-frequency converter switching and sensor noise, $P_{rms,low}$ captures the ability of the PSS to remove dominant low-frequency power oscillations caused by time-varying turbine mechanical power. Applying Eqn. (2.15) across all frequencies is equivalent to calculating the RMS of oscillating power in the time domain, given by

$$P_{rms,tot} = \sqrt{\frac{\sum_{i=1}^{L}(P_i - \overline{P})^2}{L-1}} \tag{2.16}$$

where oscillating power is defined as a time series of instantaneous power minus average power $(P - \overline{P})$.

2.3 Simulation Set-Up

The small-scale simulation of the PSS matches the topology shown in Fig. 2.9, including a controllable current source input configured to exactly match the input current I_{in} measured in benchtop PSS experiments. All component and controller parameters listed in Table 2.1 are used in the simulation (including ESRs), which is run using a fixed-step discrete solver with step size 1e-6 (selected for time-step invariance in results). This time step allows for modeling of the full switching dynamics of the system, which occurs at a much faster rate (10 kHz) than the turbine dynamics (8 Hz). The controller is configured to trigger when the PWM carrier signal is at its maximum and minimum to match the MPU configuration in hardware. In between triggers there is a zero-order hold on the measured values, capturing the effect of real-time controller delay.

To demonstrate the viability of the PSS design for a larger-scale system utilizing intracycle control, a generator-to-grid simulation is used, matching that shown in Fig. 2. The rotor speed and hydrodynamic torque inputs to the simulation are scaled from non-dimensional laboratory performance (i.e., coefficient of torque, tip-speed ratio), for a full-scale turbine with a projected frontal area of 1 m^2 operating in an inflow velocity of 2 m/s and producing an average electrical power of 1 kW. The PSS design is implemented in the same way as for the small-scale simulation, but with larger inductors and capacitors, matching available off-the-shelf components, to handle the increase in average power and a higher DC bus voltage of 480 V. A summary of the components and their estimated costs are listed in Table 2.2. Controller parameters including switching frequency, damping ratio, and bandwidth are consistent with the small-scale system, with bandwidth still equal to 10x the blade pass frequency of the turbine (1.94 Hz at larger scale). The sizing of these components is quickly determined using a linearized system, as detailed in Appendix A, which runs significantly faster than the full switched model while yielding similar results. This system uses a state-space approximation of the switched-averaged dynamics of the system, thus capturing the low-frequency dynamics while ignoring less important high-frequency switching ripple.

Table 2.2: List of controller parameters and components for the full-scale system.

Controller Parameters			
ω_o	122.2 rad/s	k_i	478 Ω
ξ	0.4	k_p	3.10 H/s^2
f_{sw}	10 kHz		

System Components				
Component	*Size*	*Rating*	*ESR [mΩ]*	*Cost*
C_1	1.93 F	480 V	720	$ 3,969
L_1	32 mH	10 A	28	$ 43
C_2	0.05 F	320 V	12	$ 557
L_2	32 mH	10 A	28	$ 43
			Total Cost	**$ 4611**

The active power delivered to the grid under intracycle control, without the PSS, is shown in Fig. 1.1. This represents a worst-case scenario of peak to average turbine power. However, we have previously demonstrated that two turbines, controlled synchronously and combined on the DC bus, improve overall turbine-to-grid system efficiency as compared to independent topology, because the intracycle phase can be coordinated such that one turbine is producing maximum power while the other is producing a minimum [14]. To simulate the double turbine case while holding power output constant, two turbines with half the projected area are used. A comparison of the performance and efficiency of the PSS for these two cases is made using the same metrics described above, averaging simulation results over eight turbine rotations. For the purpose of a direct comparison, the sizing of the inductors and capacitors is maintained in the simulation of the two systems; for a real system, the lower peak currents of the double turbine system suggests the inductor and capacitor components could be downsized, which would reduce power loss from ESR and the overall size and cost of the system.

Chapter 3

RESULTS AND DISCUSSION

3.1   Small-Scale System

A comparison between the experimental and simulated system performance is shown in Fig. 3.1. The fluctuating input power, shown in blue, is initially smoothed using the LC filter in Part I of the PSS. Here, the DC-DC converter is on, with a constant duty cycle of 0.5 holding C_2 at a steady 40 V. This allows for a smooth transition with no large current transients when the controller switches on. The Part II controller switches on midway through, varying duty cycle with turbine position to remove the remaining sinusoidal fluctuations in output power.
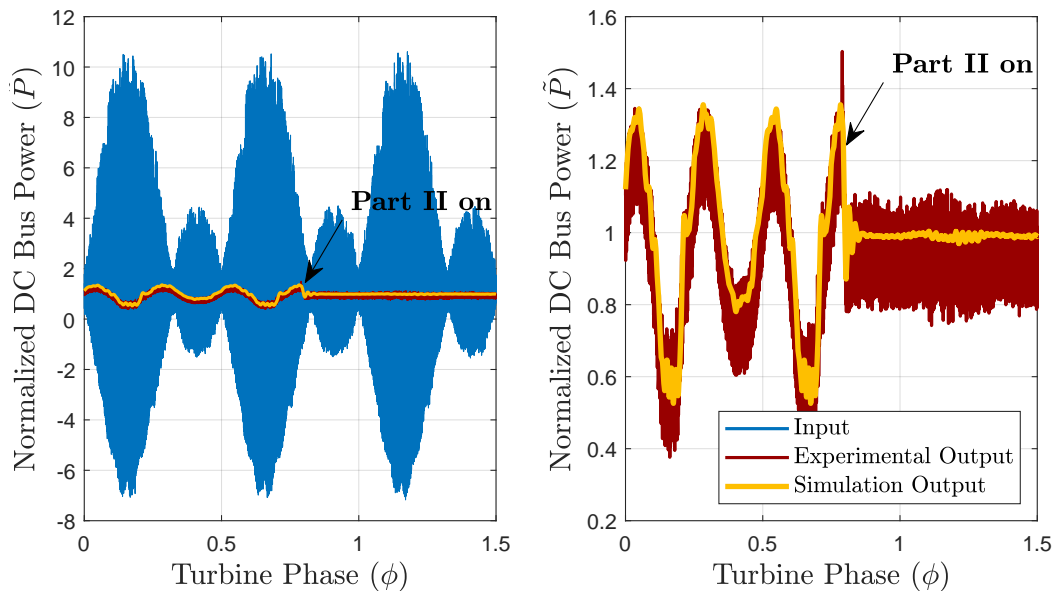

Figure 3.1: Demonstration of the PSS smoothing input power (left) and a close-up comparison between the experimental and simulated system (right).

Fig. 3.1. shows good agreement between the simulated and experimental results, with the main difference associated with high-frequency switching noise from the DC-DC converter in the experiment. This is an artifact of the prototype setup caused by switch-node ringing in the converter and could be mitigated by implementing the system on a printed circuit board, where the gate driver circuity, switches, and output capacitor could be physically located closer together to minimize parasitic inductance.

A summary of the PSS performance, comparing experimental and simulation results of system efficiency and reduction in low frequency (<100 Hz) power oscillations, is shown in Table 3.1. For PSS Part I results, PSS Part II is completely disconnected, to isolate the effect of the LC filter. Simulation shows a 98.5% reduction in RMS of undesirable low frequency oscillating power ($P_{rms,low}$) from the emulated turbine while maintaining greater than 99% efficiency. Experimental results show a slightly reduced performance, with a 94.7% reduction in $P_{rms,low}$ at 89.5% efficiency. The efficiency decrease is primarily attributable to DC-DC converter switching losses from non-zero turn-on and turn-off times. Average efficiency across the ten experimental trials is consistent, with a standard deviation of 0.023%.

Table 3.1: Comparison in small-scale PSS performance between experimental and simulated system.

System	Efficiency (η)[%]		Low-frequency RMS ($P_{rms,low}$) [W]	
	Simulation	*Experiment*	*Simulation*	*Experiment*
No PSS	100%	100%	2.37	2.37
PSS Part I	100%	99.7%	2.37	2.17
PSS Part II	99.8%	89.5%	0.034	0.130

Table 3.1 shows that PSS Part I does not significantly affect low-frequency oscillations, as expected given the LC filter cut-off frequency of 130 Hz. The ability of PSS Part II to remove low frequency power oscillations is demonstrated by the periodogram of experimental and simulation data shown in Fig. 3.2. The dominant frequencies occur at the blade passing

frequency of the turbine (8 Hz) and its harmonics. Experimental data has a higher noise floor than simulation, a consequence of converter switch-node ringing.

Part II experimental data has a dominant frequency at 10 kHz (not shown), corresponding to the switching frequency of the converter. This accounts for 65% (0.42 W) of $P_{rms,tot}$. The PSS reduces $P_{rms,tot}$ from 32 W to 0.056 in simulation and 0.65 W in experiment.
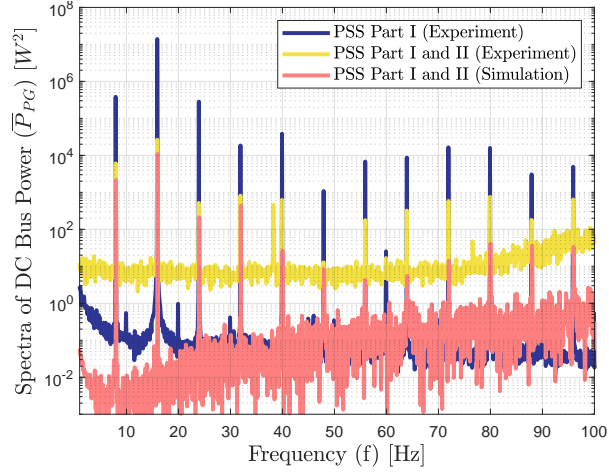

Figure 3.2: Periodogram of DC bus electrical power after utilizing the PSS.

A comparison between the reference current I_{ref} and measured current I_{L2}, for the simulation and experiment, is shown in Fig. 3.3. In both cases, the inductor current I_{L2} is measured twice per switch cycle f_{sw}, when the carrier signal is high or low and current is closest to its average value. This sampling technique allows the controller to focus on maintaining the cycle-averaged current instead of attempting to respond to highly fluctuating (and irrelevant) ripple current resulting from the charging and discharging of the inductor at the switching frequency (10 kHz).

Fig. 3.3 shows that in simulation, there is almost perfect tracking between the measured and reference current, with an RMS error of 7.1 mA, which compares favorable to the current range of 230 mA. In experiment, switch node ringing and noise leads to a larger RMS error of 32.5 mA and contributes to the poorer performance of the experimental system.

Higher switching frequency would increase controller response bandwidth and allow for easier filtering of switching noise, but would also increase switching losses and, therefore, reduce system efficiency.
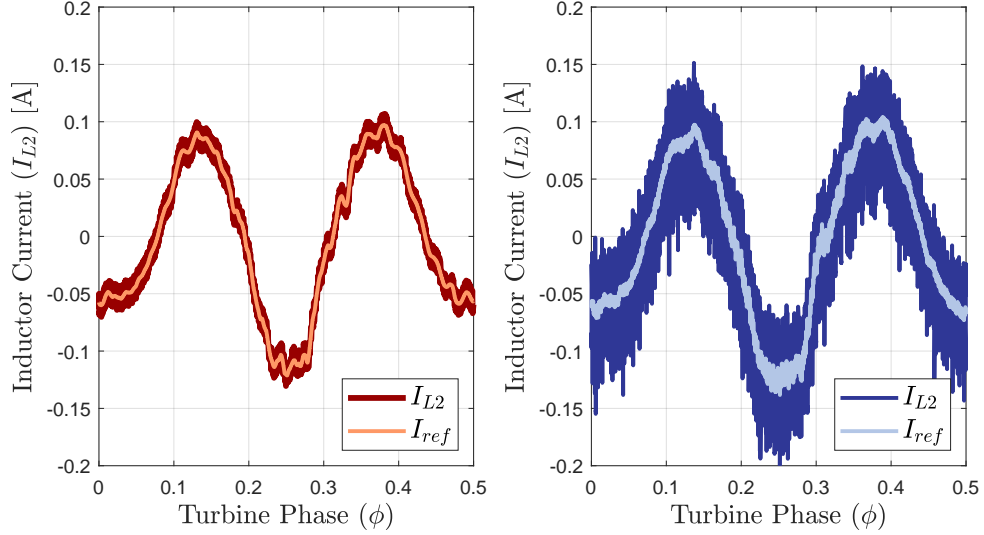
Figure 3.3: Comparison between the commanded and measured current for the simulated (left) and experimental (right) system.

3.2 Large-Scale System

Results of the large-scale PSS simulation for a single and dual turbine utilizing intracycle control are shown in Fig. 3.4. A summary of PSS performance is given by Table 3.2.

Table 3.2: Comparison in large-scale PSS performance for a single turbine and double turbine system.

System	Efficiency $(\eta)[\%]$		Low-frequency RMS $(P_{rms,low})$ [W]	
	Single	Double	Single	Double
No PSS	100 %	100 %	7130	5670
With PSS	97.0 %	98.3 %	15.1	12.3

Table 3.2 shows that for the single turbine case, low-frequency power $P_{rms,low}$ is initially 7.1 kW per cycle, 7x larger than the average power generated by the turbine. With the PSS, low-frequency power is reduced by 99.8%. This means that the inverter, transformer, and transmission line used to connect the DC bus to the utility grid could be rated to significantly lower currents than for a system without the PSS. The double turbine case has a modest 1.3% improvement in the overall efficiency of the PSS for comparable power smoothing results. This stems from the turbine power starting with a RMS of power oscillation 20% lower than the single turbine case, allowing the controller to be less aggressive.
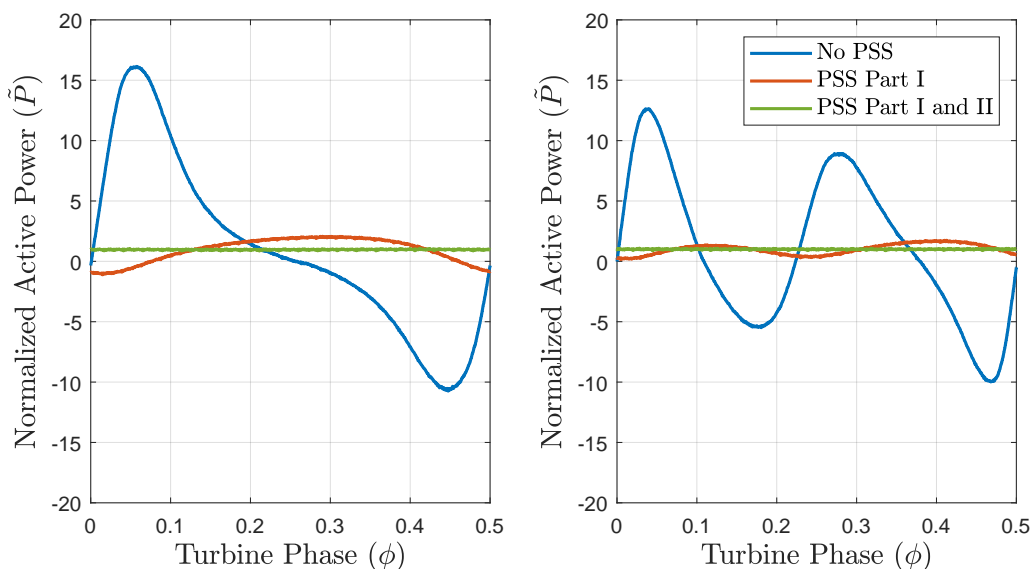
Figure 3.4: Comparison in active power delivered to the grid for a single turbine (left) and double turbine system (right) utilizing the large-scale PSS.

This is apparent in Fig. 3.5, which shows the single turbine case drawing much larger peak currents through the output capacitor and inductor of the converter (L_2 and C_2). This causes higher power losses due to the ESR of these components. Power loss from internal resistance is given by I^2R, and the single turbine case has an average value of I^2 that is 5.8x larger per cycle than the double turbine case.

Figure 3.5: Comparison in reference current for the single turbine and double turbine system. Light shading is commanded current I_{ref} and dark shading is measured I_{L2} current.
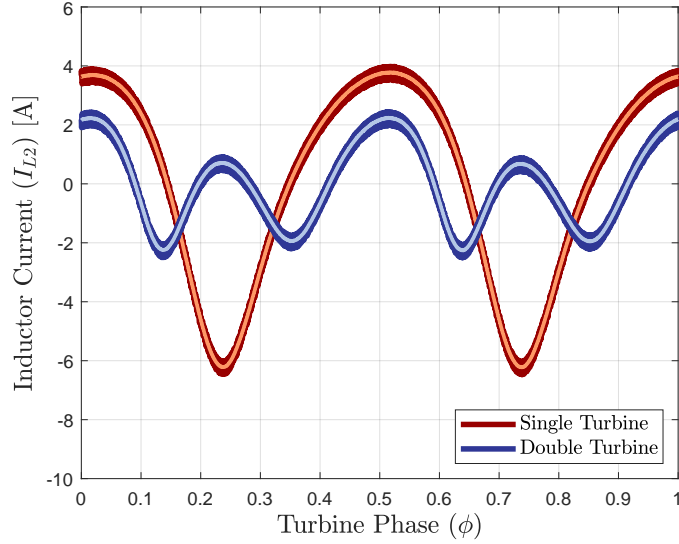
3.3 Alternative Designs

The LC filter in PSS Part I removes high-frequency variations from the current on the DC bus, giving the controller a smooth reference current to track. A potential alternative method would be to forgo the LC filter and estimate DC bus power P_{DC} using measurements on the generator side of the inverter (which does not include high-frequency switching). P_{DC} can be estimated using the dot product of back-EMF voltage V_{emf} and three phase AC current I_{abc} measured on the generator stator windings, given by

$$P_{DC} \approx V_{emf} \cdot I_{abc} \approx p\lambda\dot{\Theta} \begin{bmatrix} cos(p\Theta) \\ cos(p(\Theta - 2\pi/3)) \\ cos(p(\Theta + 2\pi/3)) \end{bmatrix} \cdot \begin{bmatrix} I_a \\ I_b \\ I_c \end{bmatrix} \tag{3.1}$$

where p is the number of generator pole pairs, λ is flux linkage, Θ is rotor position, and $\dot{\Theta}$ is rotor speed.

The power delivered to the grid when simulating the large-scale PSS with this method,

which still includes a large input capacitor C_1 but does not include L_1, is given by Fig. 3.6. Although there is good smoothing performance during part of the turbine cycle, when power changes most rapidly (at 0° and 180° of the shown turbine rotation) the system is unable to remove all oscillations in power. This suggests that there is a small delay or efficiency loss between the generator and the DC bus, creating inaccuracies in the estimated DC bus power. For turbine systems with a lower peak-to-average ratio of mechanical power, this strategy may be sufficient for power smoothing. It may be possible to predict and account for these delays or inefficiencies and consequently achieve acceptable results using this method.

This alternative would decrease the number of components and sensors needed by utilizing existing measurements, thus reducing the complexity and cost of the system. However, this method requires measurements inside the motor drive, whereas the previously described system would be entirely self-contained on the DC bus and easier to integrate with an existing system.
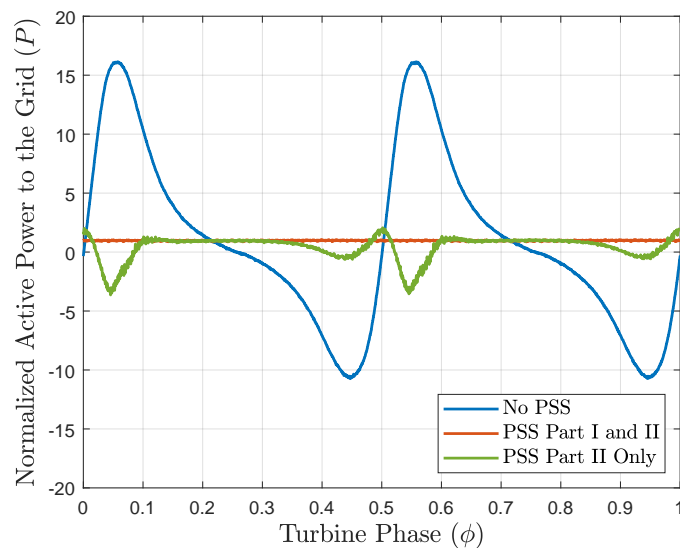

Figure 3.6: Active power to the grid for the large-scale PSS system without PSS Part I.

Chapter 4

CONCLUSION

Turbine design and control schemes used to maximize average power output may produce instantaneous power that, in its raw form, is of too poor quality to reasonably use, particularly in remote communities with weak grids. A simple power smoothing system is proposed to transform sinusoidally fluctuating power on the DC bus to steady, consistent power delivered to an end use. Regardless of the end use, whether for utility-grid integration to provide power to coastal cities, micro-grid use for remote communities, or sub-sea operations powering a single device, the high peak-to-average nature of the output power of straight-bladed cross-flow turbines will often necessitate a secondary power smoothing system. Similar power quality concerns have been noted in the wave energy sector, where power varies as a function of periodic wave height [24]. Although a slightly longer time scale (typically 0.1 Hz) than the rotation of a tidal turbine, the proposed PSS could be resized and applied to such a system. Similarly, a supercapacitor-based PSS should also be able to mitigate short-term power disturbances from turbulence for wind or current turbines. The purpose of the power smoothing system, regardless of application, is to allow the power-capturing device and control scheme to be designed with only the purpose of maximizing average power; power quality can be improved on the back-end of the conversion process with a limited efficiency penalty.

The proposed two-part system has been shown in simulation to reduce RMS of low-frequency power oscillation by 98% with negligible efficiency penalty for a laboratory-scale turbine. These results have been validated using a bench-top system, with slightly reduced performance and efficiency arising from real-world complications including switch-node ringing from parasitic inductance, switching losses from non-zero turn-on and turn-off times, and

sensor noise. A larger-scale version of the system is demonstrated in simulation for a turbine utilizing intracycle control, where RMS of oscillating grid-connected power is reduced by 99% with 3% power loss. A coordinated dual-turbine system combined on a single DC bus can further reduce power loss and PSS cost. Future work could include validating the larger-scale version of the system and deploying it in the field. Such a system could employ improved circuit design practices to mitigate many of the issues encountered at small-scale and should achieve efficiencies similar to those predicted by simulation.

BIBLIOGRAPHY

[1] Annette Evans, Vladimir Strezov, and Tim J. Evans. Assessment of utility energy storage options for increased renewable energy penetration. *Renewable and Sustainable Energy Reviews*, 16(6):4141–4147, Aug. 2012.

[2] D. Rastler. Electricity energy storage technology options: A white paper primer on applications, costs, and benefits. Technical report, Electric Power Research Institute, 2010.

[3] P. Denholm, E. Ela, B. Kirby, and M. Milligan. Role of energy storage with renewable electricity generation. Technical report, National Renewable Energy Lab, 2010.

[4] Abdul Motin Howlader, Naomitsu Urasaki, Atsushi Yona, Tomonobu Senjyu, and Ahmed Yousuf Saber. A review of output power smoothing methods for wind energy conversion systems. *Renewable and Sustainable Energy Reviews*, 26:135–146, Oct. 2013.

[5] Maider Santos-Mugica, Eider Robles, Atsede G. Endegnanew, Elisabetta Tedeschi, and Jochen Giebhardt. Grid integration and power quality testing of marine energy converters: Research activities in the marinet project. In *9th International Conference on Ecological Vehicles and Renewable Energies (EVER)*, Monte-Carlo, Monaco, Mar. 2014.

[6] Andreas Uihlein and Davide Magagna. Wave and tidal current energy a review of the current state of research beyond technology. *Renewable and Sustainable Energy Reviews*, 58:1070–1081, May 2016.

[7] Daniel Weisser and Raquel S. Garcia. Instantaneous wind energy penetration in isolated electricity grids: concepts and review. *Renewable Energy*, 30(8):1299–1308, July 2005.

[8] John Dabiri. Potential order-of-magnitude enhancement of wind farm power density via counter-rotating vertical-axis wind turbine arrays. *Renewable and Sustainable Energy Reviews*, 3(4), July 2011.

[9] Stephen Salter. Are nearly all tidal stream turbine designs wrong? In *4th International Conference on Ocean Energy*, Dublin, IR, Oct. 2012.

[10] M.J. Khan, G. Bhuyan, M.T. Iqbal, and J.E. Quaicoe. Hydrokinetic energy conversion systems and assessment of horizontal and vertical axis turbines for river and tidal applications: A technology status review. *Applied Energy*, 86(19):1823–1835, Oct. 2009.

[11] Brian Polagye, Ben Strom, Hannah Ross, Dominic Forbush, and Robert J. Cavagnaro. Comparison of cross-flow turbine performance under torque-regulated and speed-regulated control. *Journal of Renewable and Sustainable Energy*. (in the press).

[12] Ben Strom, S L. Brunton, and Brian Polagye. Consequences of preset pitch angle on cross-flow turbine hydrodynamics. In *11th European Wave and Tidal Energy Conference*, Nantes, FR, Sept. 2015.

[13] B. Strom, S L. Brunton, and B. Polagye. Intracycle angular velocity control of cross-flow turbines. *Nature Energy*, 2, May 2016.

[14] R. J. Cavagnaro, B. Strom, B. Polagye, and A. Stewart. Power collection from multiple hydrokinetic generators utilizing advanced control. In *12th European Wave and Tidal Energy Conference*, Cork, IR, Aug. 2017.

[15] H. Ibrahim, A. Ilinca, and J. Perron. Energy storage systems —characteristics and comparisons. *Renewable and Sustainable Energy Reviews*, 12(5):1221–1250, June 2008.

[16] Zhibin Zhou, Mohamed Benbouzid, Jean Frdric Charpentier, Franck Scuiller, and Tianhao Tang. Energy storage technologies for smoothing power fluctuations in marine current turbines. In *IEEE International Symposium on Industrial Electronics*, Hangzhou, China, Nov. 2012.

[17] Kodai Ushiwata, Seiji Shishido, Rion Takahashi, Toshiaki Murata, and Junji Tamura. Smoothing control of wind generator output fluctuation by using electric double layer capacitor. In *International Conference on Electrical Machines and Systems*, Seoul, Korea, Oct. 2007.

[18] A. Abedini and A. Nasiri. Applications of super capacitors for pmsg wind turbine power smoothing. In *34th Annual Conference of IEEE Industrial Electronics*, Orlando, Florida, Nov. 2008.

[19] J. Staiger, S. Bosch, and H. Steinhart. Application of a buck-boost converter for highly dynamic power smoothing in industrial applications. In *Power Conversion and Intelligent Motion Conference*, Nuremberg, DE, May 2017.

[20] Robert W. Erickson and Dragan Maksimovic. *Fundamentals of Power Electronics*, pages 331–376. Kluwer, 2 edition, 2004.

[21] Dominic Forbush, Robert J. Cavagnaro, James Donegan, Jarlath McEntee, and Brian Polagye. Multi-mode evaluation of power-maximizing cross-flow turbine controllers. *International Journal of Marine Energy*, 20:80–96, Dec. 2017.

[22] L. Jin and S. Chan. A unified and efficient approach for determining thevenin (norton) equivalent circuits. *IEEE Transactions on Education*, 32(3):408–410, Aug. 1989.

[23] William H. Press, Saul A. Teukolsky, William T. Vetterling, and Brian P. Flannery. *Numerical Recipes in C*, pages 549–558. Cambridge University Press, 2 edition, 1992.

[24] H. Polinder and M. Scuotto. Wave energy converters and their impact on power systems. In *International Conference on Future Power Systems*, Amsterdam, NL, 2017.

Appendix A

TURBINE SET-UP

Although emulating the DC bus in hardware and using the expected electrical power output from a flume-scale turbine as the input is sufficient to validate simulation results, using a real turbine to produce electrical power and implement the PSS on this output power would be a more meaningful test of the system. An attempt at such a system was made, however it was found difficult to select system components (e.g., generator) that resulted in net electrical power generation from the laboratory-scale turbine.

Fig. A.1 shows the turbine set-up in the flume, which is mounted from both ends (using a vacuum plate for the bottom mount), a servo motor, top and bottom load cells, and a bottom bearing. The topology of a typical full flume-scale system is shown in Fig. A.2, where the motor drive houses the inverter, DC bus, and rectifier.

Unfortunately, the topology shown in Fig. A.2 does not work to validate the electrical simulation results, because the DC bus is entirely hidden inside the motor drive. Therefore, an alternative system was developed which uses a motor drive powered by a DC power supply, as shown in Fig A.3. This system allows regenerated power from the turbine to be output back onto the DC bus, as would also happen in a full-scale grid-connected scenario. The PSS could then be implemented on the DC bus, as is done in simulation.

The disadvantage of such as system is that generators and motor drives of this size are not typically designed to efficiently regenerate electrical power. The servomotor used to control the turbine is a Parker SM233AL-KPSN, which has a rated speed of 3000 RPM. A turbine of this scale is rotated at approximately 200 RPM to achieve an optimal tip speed ratio, approximately 7% of the servomotor's rated speed. Therefore, the generator coils are oversized for this application and do not efficiently convert mechanical to electrical power

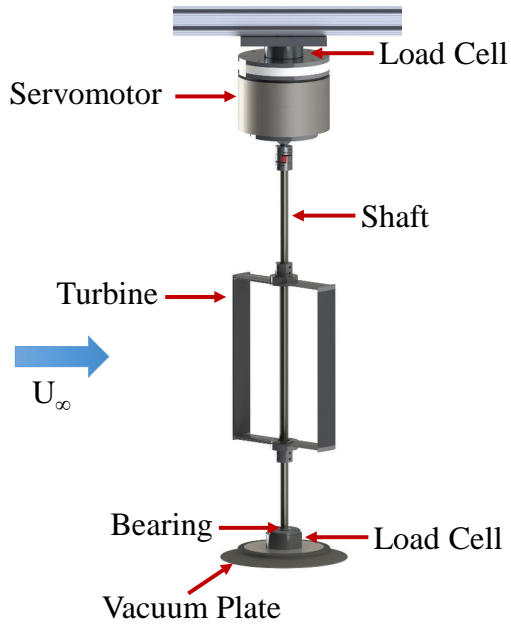(i.e., most of the mechanical power produced by the turbine is converted to heat from winding losses).

Figure A.1: Turbine test set-up in a recirculating flume, with freestream flow defined as U_∞.
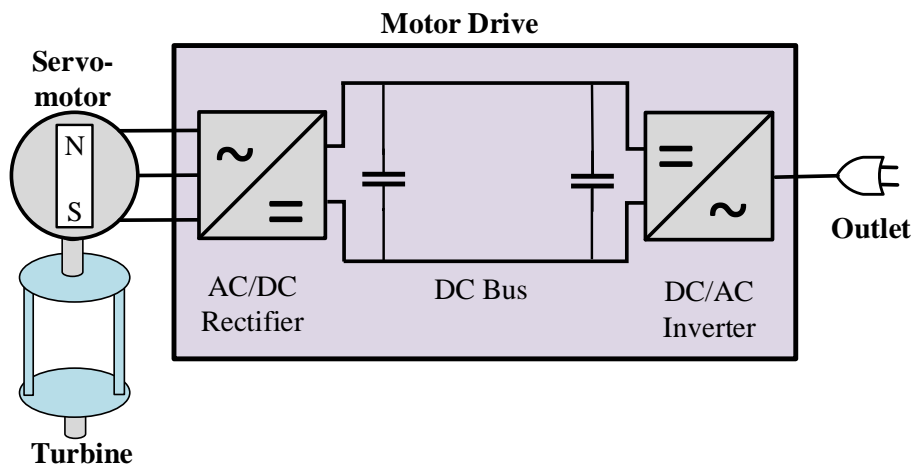

Figure A.2: Typical flume-scale turbine system set-up, where the DC bus is housed inside the motor drive.
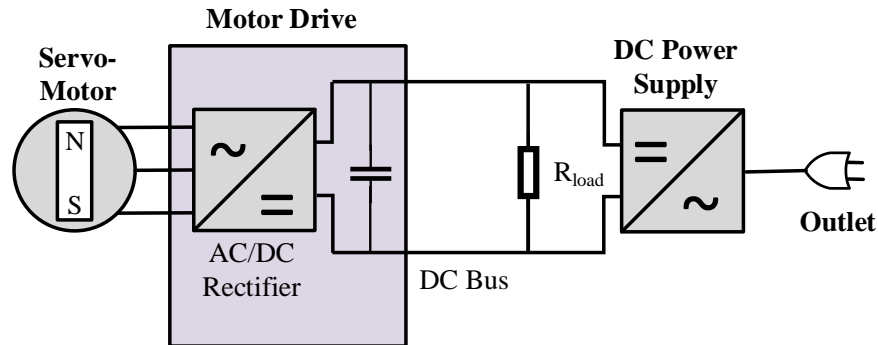
Figure A.3: Modified flume-scale turbine system, with DC bus external to the motor drive.

The motor drive used is Advanced Motion Controls DPRALTE-020B080, which uses a rectifier to convert the DC power input into three phase AC power connected to the servomotor. The current in the stator windings is regulated by the motor drive to achieve the desired rotor speed. This drive has the unique capability of being able to regenerate power externally back onto the DC bus, the same input which is being used to power the drive. For an ideal system with no losses, the mechanical power produced from the turbine would be perfectly converted into an equal amount of electrical power in three phase AC inside the motor, then from AC to DC power on the DC bus using the motor drive.

However, because the real system departs from this idealization and the power output from the laboratory scale turbine is relatively small, net power generation is not possible. The drive itself requires around 5 W for internal loads, and the servomotor's mechanical to electrical efficiency is approximately 30% across a range of turbine speeds at a free-stream flow speed of 1 m/s (the maximum allowable in the flume). The maximum mechanical power of the laboratory-scale turbine is around 7 W, for an optimal tip-speed ratio of 2.1. Fig. A.4 compares the mechanical power produced from the turbine over a range of tip speed ratios, as compared to the electrical power measured on the DC bus.

As shown by Fig. A.4, the average power regenerated by the turbine onto the DC bus is negative. It is impossible to implement the PSS system for a system that consumes power, since the system is designed to smooth power in one direction on the DC bus (from the

turbine side to the grid side). It may be possible to increase the electrical power output by making altercations to the system, including adding a gearbox to increase the speed of the generator rotor to improve mechanical to electrical efficiency, using a drive which separates its logic and motor power, using a larger turbine, and using a flume capable of higher flow speeds. Through these methods it is likely possible to achieve average positive power on the DC bus and and implement the PSS on a small-scale turbine. Such as system could be used to validate simulation results or power small devices such as oceanographic sensors.
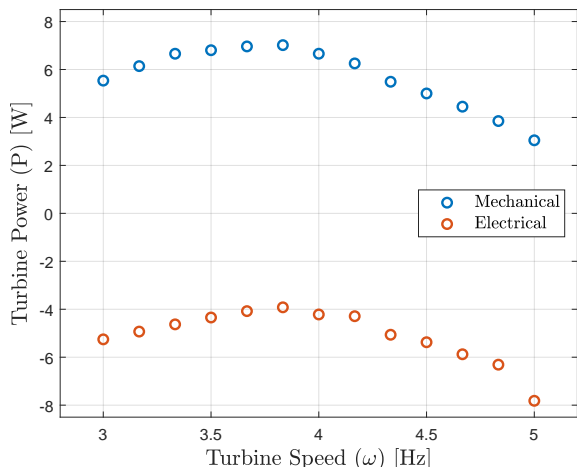

Figure A.4: Average mechanical and electrical power of flume-scale turbine across an range of turbine speeds.

Because the experimental system proved difficult to set up, the input to an emulated system was created based on a simulation of a small-scale turbine generator modeling the conversion between mechanical and electrical power. This simulation result gives an estimate of the electrical power on the turbine DC bus. The purpose of the experimental PSS system is to show that for a given electrical power input, it can smooth power appropriately, and the experimental results match simulation results using the same input. The exact electrical input itself is less relevant to the results. Using a differently sized generator may shift or stretch the simulated output current, but should not change the overall shape significantly, and should not effect the overall results of the small-scale PSS.

Appendix B

SYSTEM LINEARIZATION

The simulation discussed in 2.3 uses a full switched model of the system, which provides the most accurate results but is also time consuming to run and computationally expensive. An alternative linearized system of the switched model is presented here, reducing the entire system "Plant" to six differential equations. This linearized plant model, coupled with the same controller model, provides nearly equivalent predicted performance, while neglecting the high frequency switching dynamics present in the real system.

To create a linearized model, the two possible configurations of the DC-DC converter are considered. Configuration A corresponds to switch Q_1 on and Q_2 off; Configuration B corresponds to the opposite scenario of Q_1 off and Q_2 on. The duty cycle D defines the percentage of each switch cycle the converter is in Configuration A, and $D' = 1 - D$ is the percentage of time it is in Configuration B. The two switches are controlled synchronously such that the converter will always either be in Configuration A or Configuration B ($D + D' = 1$). Configuration A is shown on the left-hand side of Fig. B.1 and Configuration B is shown on the right.
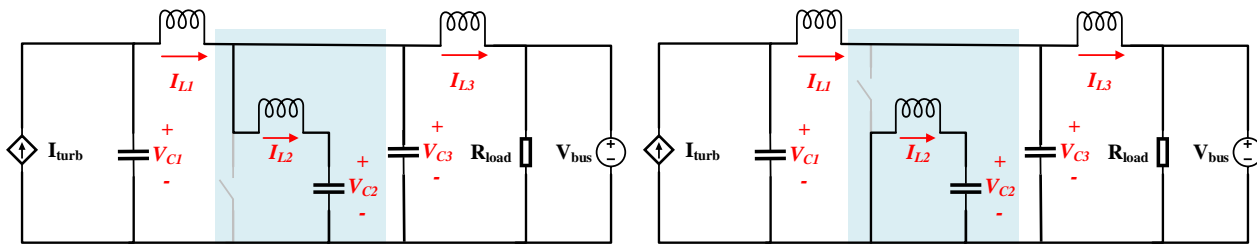

Figure B.1: Configuration A (left) and Configuration B (right) of the switching converter.

For each configuration, a differential equation is written for each of the six state variables. State variables are the inductor currents and capacitor voltages, as labeled in Fig. B.1. The differential equations for Configuration A are collectively referred to as $\dot{x_A}$ and for Configuration B as $\dot{x_B}$. These differential equations are written using Kirchhoff's Current Law, Kirchhoff's Voltage Law, and equations relating current and voltage across a capacitor and inductor, given by

$$V_L = L\frac{dI_L}{dt} \tag{B.1}$$

$$I_C = C\frac{dV_C}{dt} \tag{B.2}$$

where V_L is inductor voltage, I_L is inductor current, V_C is capacitor voltage, I_C is capacitor current, L is inductance, and C is capacitance.

An equation governing the average dynamics of each differential equation can be written based on the duty ratio D. Terms which appear in the $\dot{x_A}$ equations are multiplied by D, and terms which appear in the $\dot{x_B}$ equations are multiplied by $1 - D$, given by

$$\dot{x} = D\dot{x_A} + (1 - D)\dot{x_B}. \tag{B.3}$$

The six governing equations for the linearized switched averaged model of the system are given by

$$\dot{x} = \begin{bmatrix} \dot{I_{L1}} \\ \dot{I_{L2}} \\ \dot{I_{L3}} \\ \dot{V_{C1}} \\ \dot{V_{C2}} \\ \dot{V_{C3}} \end{bmatrix} = \begin{bmatrix} \frac{1}{L_1}(V_{C1} - V_{C3} - R_{L1}I_{L1}) \\ \frac{1}{L_2}(DV_{C3} - V_{C2} - R_{L2}I_{L2}) \\ \frac{1}{L_3}(V_{C3} - V_{bus} - R_{L3}I_{L3}) \\ \frac{1}{C_1}(I_{in} - I_{L1}) \\ \frac{1}{C_2}I_{L2} \\ \frac{1}{C_3}(I_{L1} - DI_{L2} - I_{L3}) \end{bmatrix} \tag{B.4}$$

which includes inductor internal series resistances R_L. The equations for $\dot{I}_{L1}$, $\dot{I}_{L3}$, $\dot{V}_{C1}$, and $\dot{V}_{C2}$ are identical between the two states, whereas the equations for $\dot{I}_{L2}$ and $\dot{V}_{C3}$ change based on the converter state and are therefore dependent on the duty cycle D. A linearized state space form of the system can be written using

$$\dot{x} = A[x - X] + B[u - U] \tag{B.5}$$

where x are the state equations and u are the system inputs,

$$x = \begin{bmatrix} I_{L1} \\ I_{L2} \\ I_{L3} \\ V_{C1} \\ V_{C2} \\ V_{C3} \end{bmatrix}, u = \begin{bmatrix} I_{in} \\ V_{bus} \\ D \end{bmatrix} \tag{B.6}$$

where I_{in} is the input current to the system, V_{bus} is the the DC bus voltage, and D is the duty ratio. A is defined as the Jacobian matrix of $\dot{x}$ with respect to the state variables, and B is the Jacobian matrix with respect the input variables, given by

$$A = \begin{bmatrix} \frac{\partial f_1}{\partial x_1} \cdots \frac{\partial f_1}{\partial x_N} \\ \vdots \\ \frac{\partial f_N}{\partial x_1} \cdots \frac{\partial f_N}{\partial x_N} \end{bmatrix}_{X, U} = \begin{bmatrix} -\frac{R_{L1}}{L_1} & 0 & 0 & \frac{1}{L_1} & 0 & -\frac{1}{L_1} \\ 0 & -\frac{R_{L2}}{L_2} & 0 & 0 & -\frac{1}{L_2} & \frac{D}{L_2} \\ 0 & 0 & -\frac{R_{L3}}{L_3} & 0 & 0 & \frac{1}{L_3} \\ -\frac{1}{C_1} & 0 & 0 & 0 & 0 & 0 \\ 0 & \frac{1}{C_2} & 0 & 0 & 0 & 0 \\ \frac{1}{C_3} & -\frac{D}{C_3} & -\frac{1}{C_3} & 0 & 0 & 0 \end{bmatrix} \tag{B.7}$$

$$B = \begin{bmatrix} \frac{\partial f_1}{\partial u_1} \cdots \frac{\partial f_1}{\partial u_M} \\ \vdots \\ \frac{\partial f_N}{\partial u_1} \cdots \frac{\partial f_N}{\partial u_M} \end{bmatrix} \Bigg|_{\text{X, U}} = \begin{bmatrix} 0 & 0 & 0 \\ \frac{V_{C3}}{L_2} & 0 & 0 \\ 0 & -\frac{1}{L_3} & 0 \\ 0 & 0 & \frac{1}{C_1} \\ 0 & 0 & \frac{1}{C_1} \\ -\frac{I_{L2}}{C_3} & 0 & 0 \end{bmatrix}. \tag{B.8}$$

The equilibrium point X is calculated by setting Eqn. (B.4) equal to zero and solving for the state variables, given by

$$X = \begin{bmatrix} \mathbf{I_{L1}} \\ \mathbf{I_{L2}} \\ \mathbf{I_{L3}} \\ \mathbf{V_{C1}} \\ \mathbf{V_{C2}} \\ \mathbf{V_{C3}} \end{bmatrix} = \begin{bmatrix} \mathbf{I_{in}} \\ 0 \\ \mathbf{V_{bus}} + \mathbf{I_{in}} R_{L1} + \mathbf{I_{in}} R_{L3} \\ \mathbf{D}(\mathbf{V_{bus}} + \mathbf{I_{in}} R_{L3}) \\ \mathbf{V_{bus}} + \mathbf{I_{in}} R_{L3} \\ \mathbf{V_{C3}} \end{bmatrix} \tag{B.9}$$

where time-averaged constant terms are denoted in bold (time-varying terms are not bolded as shown in previous equations). U is defined as the initial conditions for the system, given by

$$U = \begin{bmatrix} \mathbf{I_{in}} \\ \mathbf{V_{bus}} \\ \mathbf{D} \end{bmatrix} = \begin{bmatrix} 0.134 \\ 80 \\ 0.5 \end{bmatrix}. \tag{B.10}$$

To solve this linearized system, a closed loop block diagram model is created in Simulink, similar to the full switching model except that the "Plant" of inductive, capacitive, and switching components is replaced by the state space model given by Eqn. (B.5). The appropriate inductor currents and capacitor voltages output from the plant are fed into the

controller, which calculates a reference current based on the current and voltage on the DC bus (I_{L2} and V_{C3}) and the voltage across the capacitor, V_{C2}. This reference current is compared to the actual current, I_{L2}, and the difference between the two is fed into a PI controller to calculate a duty cycle D. D becomes an input to the plant model, controlling the plant in real-time. I_{in} is a time series of input current matching that shown in Fig. 2.6, and V_{bus} is set at 80 V. A simplified model of the system is shown in Fig. B.2. All capacitor, inductor, and inductor ESR values match that given in Table 2.1. This model is implemented in Matlab Simulink with a discrete step solver with time step of 1e-5 s, chosen as an optimal middle ground between fast run time and accurate results.
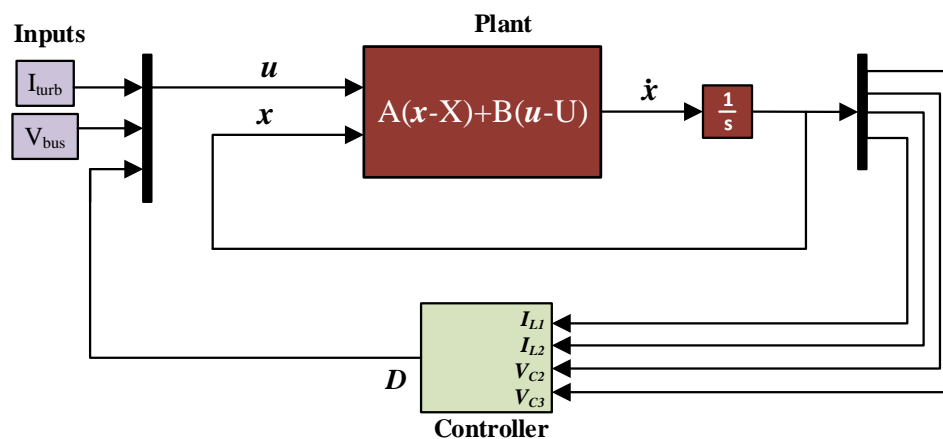

Figure B.2: Linearized state space model simulation layout.

The full switched model simulation used to compare to this linearized model is almost identical to the system described in Section 2.3, with a time step of 1e-6 s. The only difference is that the controller operates continuously, to observe how capturing the full switching dynamics of the system compares with the switch cycle-averaged linearized model.

A comparison of the power output for the linearized model and switching model are shown in Fig. B.3. The results show strong agreement between the two models; even the transient period when PSS Part II switches on is well-described by the linearized system.
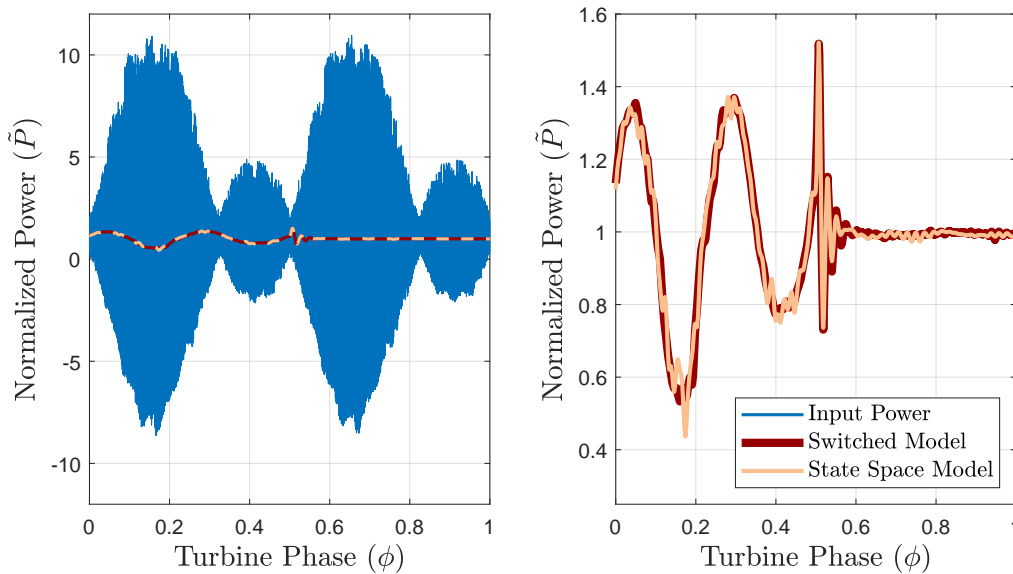
Figure B.3: Comparison in input and output power for the linearized and switched model.

A comparison between the reference current and measured current for the two models is shown in Fig. B.4. The reference current between the two models is again almost identical. As expected, the two models differ in how they capture the inductor current I_{L2}. The switched model captures the full ripple current through the inductor as the DC-DC converter alternates between its switch states, while the linearized model only tracks the average current.

Similar results are seen by comparing duty ratio and capacitor voltage V_{C2}. The duty cycle of the switched model is responding to inductor ripple current, while the state space model is cycle-averaged. Capacitor voltage shows almost perfect tracking between the two models.

These results show that the linearized state space model is a robust representation of the full switched model, while running at 10x the speed. This suggests that the linearized model is a good starting point for sizing a new system; it can provide confirmation that the chosen component parameters (L's and C's) and controller gains (k_p and k_i) are sufficient

to smooth power appropriately. Once a system is created in the linearized domain, it can be transferred to the full switched model, which will have a longer run time but more accurately capture real system dynamics.
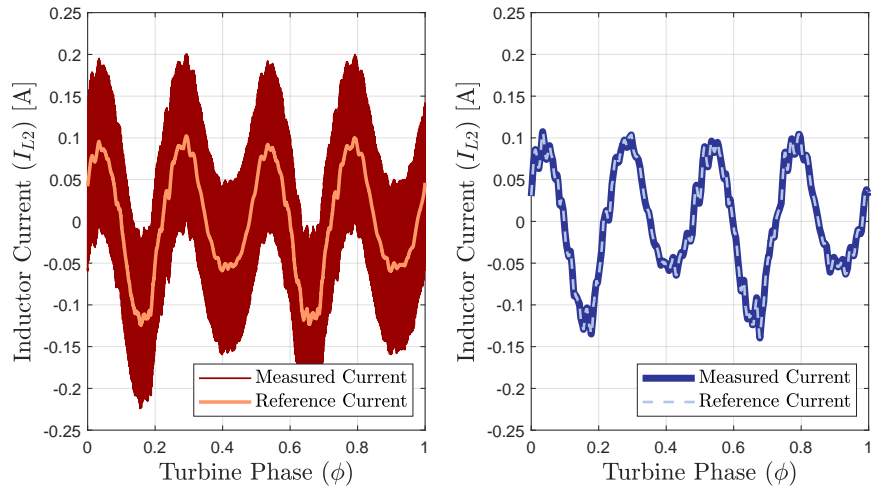

Figure B.4: Comparison between reference current and true current for the switched (left) and linearized (right) model.
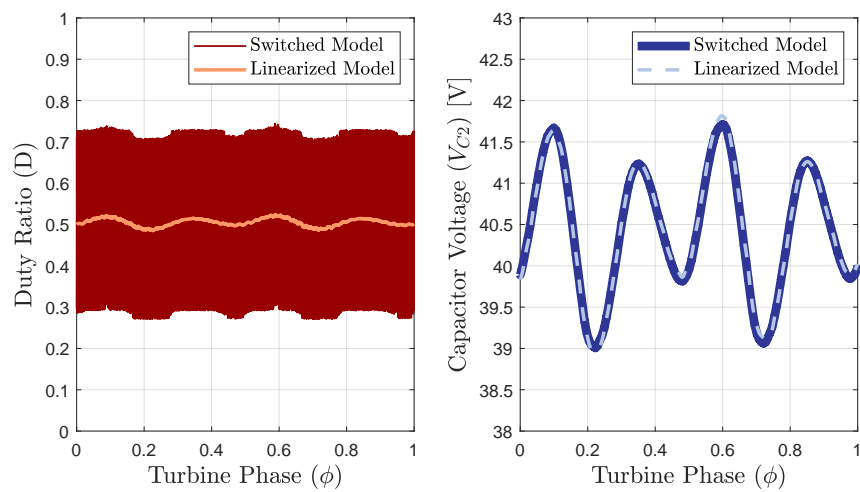

Figure B.5: Comparison between duty ratio (left) and capacitor voltage (right) for the switched and linearized model.

VITA

Hannah Aaronson completed this work as an associate researcher for the Pacific Marine Energy Center at the University of Washington in Seattle, Washington. Upon graduation, she will be working as senior personnel for Hive Battery Labs, a start-up company based out of Seattle working to alleviate bottlenecks in battery testing by utilizing battery impedance spectroscopy.